

Experimental Quantum Imaging exploiting multi-mode spatial correlation of twin beams

Giorgio Brida, Marco Genovese, A. Meda, Ivano Ruo Berchera^{*1}

¹*INRIM, strada delle Cacce 91, 10135 Torino, Italy.*

Properties of quantum states have disclosed new and revolutionary technologies, ranging from quantum information to quantum imaging. This last field is addressed to overcome limits of classical imaging by exploiting specific properties of quantum states of light. One of the most interesting proposed scheme exploits spatial quantum correlations between twin beams for realizing sub-shot-noise imaging of weak absorbing objects, leading ideally to a noise-free imaging. Here we discuss in detail the experimental realization of this scheme, showing its capability to reach a larger signal to noise ratio with respect to classical imaging methods and, therefore, its interest for future practical applications.

PACS numbers: 42.50.Ar, 42.50.Dv, 42.50.Lc, 03.65.Wj

I. INTRODUCTION

The possibility of manipulating quantum states as atoms, photons, etc. has recently fostered the developing of quantum technologies [1–18], with very promising opportunities for future widespread applications. Among quantum technologies the ones based on photons, in particular exploiting entanglement as a resource, have produced the most impressive results, such as quantum cryptography [2, 3], teleportation [4–6], linear-optics quantum computation [7], entanglement distillation [8] and purification [9–11], quantum metrology [17]. The use of quantum properties of light for overcoming limits of classical imaging is one of the most promising [12–14]. In particular it was suggested that, by exploiting the strong correlation in noise of entangled modes of light produced by Parametric Down Conversion (PDC), the image of a weak absorbing object in one branch, eventually previously hidden in the noise, can be restored by subtracting the spatial noise pattern measured in the other branch, a technique that has been christened Sub Shot Noise Quantum Imaging (SSNQI) [23]. When operating under shot noise regime (avoiding the limits of the need of background subtraction [24] or single spatial mode operation [19–21, 31]) the method allows in principle a full reconstruction of the absorption pattern of an object with a sensitivity superior to that available with classical techniques at the same illumination level. In order to reach this goal in view of important practical applications one should reach a very high level of spatial quantum correlation. In [23] we have demonstrated that this level can be effectively reached and, then, in [25] we have presented a proof of principle of the sub shot noise quantum imaging scheme. Here, in order to provide all the necessary information, we present further data, discussing the details of the experimental realization. In particular, we show how to reach a degree of spatial correlation needed for SSNQI performances better than the corresponding classical scheme, i.e. a differential classical imaging (DCI) scheme in which, instead of the twin beams of PDC, two classically correlated beam are used. This achievement

demonstrates that an experimental setup for SSNQ imaging is feasible and the practical application of the method can be upcoming. In Sec.II we provide a basic introduction to the multi-mode spatial squeezing and the idea of SSNQI exploiting PDC, while Sec.III describes the experimental set-up and the spatial sub-shot-noise measurements. Sec.IV considers some effects that spoil the spatial sub-shot-noise regime and their possible corrections. Finally, in Sec.V we present our quantum imaging experiment, and two different figures of merit that compare the performances of SSNQI and DCI. Some conclusion and remarks can be found in Sec.VI

II. THE SCHEME

The scheme [14] for achieving quantum imaging of weak absorbing objects, is based on considering two spatially correlated areas of Parametric Down Conversion (PDC) light. This is a non-linear optical phenomenon [1, 18] where a pump beam photon "decays" in two lower frequencies photons, usually called signal (s) and idler (i), strongly correlated in frequency and momentum since they have to conserve the energy and momentum of the original pump photons. In particular, the conservation of the transverse (to the propagation direction) component of the momentum traduces in a correlation between the photon number $N_i(\mathbf{x})$ and $N_s(-\mathbf{x})$ ideally detected in any pairs of symmetrical positions \mathbf{x} and $-\mathbf{x}$ in the far field plane (note: we restrict to wavelength near degeneracy wavelength $\lambda_s = \lambda_i$). The degree of correlation is quantified by the Noise Reduction Factor (NRF)

$$\begin{aligned} \sigma &\equiv \frac{\langle \delta^2(\hat{N}_i - \hat{N}_s) \rangle}{\langle \hat{N}_i + \hat{N}_s \rangle} \\ &= \frac{\langle \delta^2 \hat{N}_s \rangle + \langle \delta^2 \hat{N}_i \rangle - 2\langle \delta \hat{N}_s; \delta \hat{N}_i \rangle}{\langle \hat{N}_s + \hat{N}_i \rangle}, \end{aligned} \quad (1)$$

where $\langle \delta^2 \hat{O} \rangle = \langle \hat{O}^2 \rangle - \langle \hat{O} \rangle^2$ is the mean square fluctuation of a generic operator \hat{O} . The normalization in Eq. (1) represents the Shot Noise Limit (SNL) $\langle \hat{N}_s + \hat{N}_i \rangle$, defined as the level of fluctuation associated to the difference between coherent beams. In terms of the transmission η of the optical channel (including the quantum efficiency of the detector) the theoretical value of NRF for PDC is $\sigma = 1 - \eta$ (considering for simplicity balanced losses $\eta_s = \eta_i = \eta$ that leads to symmetrical statistical properties of the detected beams). Therefore, in an ideal case in which $\eta \rightarrow 1$, σ approaches zero. On the other side, for the subtraction of two classical beams the degree of correlation is bounded by $\sigma_{class} \geq 1$, where the lowest limit $\sigma_{class} = 1$ is reached for coherent beams, or correlated beams, generated by a single classical beam separated by a balanced beam splitter. In this case the subtraction of the detected intensities allows to eliminate the classical excess noise contained in the source, while the shot noise survives, leading to $\langle \delta^2(\hat{N}_i - \hat{N}_s) \rangle = 2\langle \hat{N}_s \rangle$. The idea of sub-shot noise quantum imaging (SSNQI), depicted in Fig. 1, consists in measuring the intensity pattern on one branch (e.g. the signal one), where the object has been inserted, and then subtracting the correlated noise pattern measured in the other branch (the idler one) that does not interact with the object. The number of photon detected in presence of the object in the signal region is $\langle N'_s(\mathbf{x}) \rangle = [1 - \alpha(\mathbf{x})]\langle N_s \rangle$ where $\alpha(\mathbf{x})$ is the absorption in the position \mathbf{x} .

Therefore, in the SSNQI scheme we evaluate the absorption as

$$\alpha(\mathbf{x}) = \langle [N_i(-\mathbf{x}) - N'_s(\mathbf{x})] \rangle / \langle N_i \rangle \quad (2)$$

where implicitly we always consider $\langle N_i \rangle = \langle N_s \rangle$.

The Signal to Noise Ratio (SNR) is improved because the spatial noise that affects the single beam is washed away by the subtraction. In Ref.[14] the theoretical capability of the described method exploiting PDC has been compared with the ones of the corresponding differential classical scheme in which a coherent beam is split by a 50% beam splitter. It was shown that this leads to a ratio between the SNR in quantum and in the differential classical imaging of

$$R^{DCI} = \frac{SNR_{SSNQI}}{SNR_{DCI}} = \sqrt{\frac{(2 - \alpha)}{\alpha^2 E_n + 2\sigma(1 - \alpha) + \alpha}} \quad (3)$$

for the same number of photons. We have introduced the excess noise $E_n = (\langle \delta^2 N_i \rangle - \langle N_i \rangle) / \langle N_i \rangle$ of the PDC, i.e. the noise that exceeds the SNL, also referred to as standard quantum limit. For multi-thermal statistics of the single branch of PDC light, the excess noise is roughly given by $\langle N \rangle / \mathcal{M}$, with \mathcal{M} the number of modes. Equation 3 shows that, when the excess noise is negligible (in particular $\alpha^2 E_n \ll 1$), the SSNQI presents an advantage respect to a classical differential imaging for a weak absorbing object ($\alpha \rightarrow 0$) as soon as $\sigma < 1$. This for-

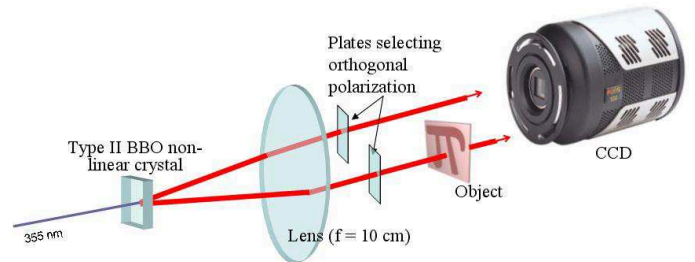


FIG. 1: Experimental set up. A 355 nm laser beam pumps a type II BBO crystal producing PDC. After eliminating UV beam, one correlated beam cross a weak absorbing object and it is addressed to a CCD array. The other beam (reference) is directly addressed to another area of CCD camera. The total transmittance of the optical path is evaluated to 70%.

mula can be generalized to the case of multi-thermal super Poissonian source for the differential classical scheme (instead of only considering coherent light) just including in the numerator under square root the term $E_n^{class} \alpha^2$, that represents the contribution due to the excess noise E_n^{class} of the classical light.

Furthermore, it can be demonstrated that for $\sigma < 0.5$ the quantum imaging technique is more advantageous than an ideal direct classical scheme, and therefore it can be a useful resource for practical applications [26].

III. THE EXPERIMENTAL REALIZATION OF THE SUB-SHOT-NOISE

In our experimental setup a type II BBO non-linear crystal ($l = 7$ mm) is pumped by the third harmonic (355 nm) of a Q-switched Nd:Yag laser. The pulses have a duration of $T_{pump} = 5$ ns with a repetition rate of 10 Hz and a maximum energy, at the selected wavelength, of about 200 mJ. This choice for the pulse duration is motivated by the indications of Ref. [14] for realizing a set-up suited for a test of SSNQI, overcoming the limits of Ref. [24]. After eliminating with a prism the residual of first and second harmonic components, the pump beam crosses a spatial filter (a lens with a focal length of 50 cm and a diamond pin-hole, 250 μm of diameter), in order to eliminate the non-gaussian components and then it is collimated by a system of lenses to a diameter of $w_p = 1.25$ mm. After the crystal, the pump is stopped by a couple of UV mirrors, transparent to the visible (T=98% at 710 nm), and by a low frequency-pass filter (T=95% at 710 nm). The down converted beams

(signal and idler) are separated in polarization by two polarizers ($T=97\%$) and finally the far field is imaged by a CCD camera 1. We used a 1340X400 CCD array, Princeton Pixis:400BR (pixel size of $20\ \mu\text{m}$), with high quantum efficiency (around 80%) and low noise in the read out process ($\Delta = 4$ electrons/pixel). The CCD exposure time is set by a mechanical shutter to 90 ms, thus each image cached in this time window corresponds to the PDC emission generated by a single shot of the laser. The far field is observed at the focal plane of the lens ($f = 10$ cm) in a $f - f$ optical configuration, ensuring that we image the Fourier transform of the crystal exit surface. Therefore, a single transverse mode \mathbf{q} of the down converted photons is associated to a single point $\mathbf{x} = (\lambda f/2\pi)\mathbf{q}$ of the image.

We expect a strict correlation in the number of photons \hat{N}_i and \hat{N}_s detected at any couple of symmetric positions with respect to the center of symmetry, providing the detection areas are larger than the typical coherence area [23]. The coherence area \mathcal{A}_{coh} , i.e. the uncertainty on the relative position of the correlated photons in the far field, depends on the pump angular bandwidth [14], and on the parametric gain [27, 28]. In our framework the detectors are the pixels of the CCD array and therefore the single pixel should be of the same order of magnitude of the coherence area or bigger. By contrary, if the pixel is smaller, the photons detected at the pixel in the position \mathbf{x} will have the correlated ones spread on several pixels around the position $-\mathbf{x}$. This spoils the pixel-pixel correlation.

For this reason, and in order to reduce the contribution of the read noise of the CCD, it is convenient to perform an hardware binning of the physical pixels. It consists in grouping the physical pixels in squared blocks $N_x N_y$, each of them being processed by the CCD electronics as single "superpixel" (the photons collected by the superpixel are the sum of the photons of each pixel, whereas the read noise is just slightly increased with respect the one of the single pixel). As described in [23], following the previous argumentation, the size of the superpixel \mathcal{A}_{pix} must be at least of the order of the coherence area, although the ideal condition is $\mathcal{A}_{pix}/\mathcal{A}_{coh} \gg 1$. In the present paper we consider three different superpixel sizes: 12×12 , 24×24 and 32×32 , being the measured coherence area $\mathcal{A}_{coh} \sim (6\ \text{pixel})^2 = (120\ \mu\text{m})^2$.

The number of temporal modes collected in one shot image is $\mathcal{M}_{temp} = (T_{pump}/T_{coh}) \sim 5 \cdot 10^3$, estimating the coherence time T_{coh} of the PDC process around one picosecond [1]. The number of spatial modes collected by the superpixel is $\mathcal{M}_{spatial} \sim \mathcal{A}_{pix}/\mathcal{A}_{coh}$ depends only on its size, since \mathcal{A}_{coh} is fixed by the pump transverse size. From the total number of modes $\mathcal{M} = \mathcal{M}_{temp} \otimes \mathcal{M}_{spatial} \sim 10^4 \div 10^5$ and the mean photon number per pixel one expect the excess noise of the multi-thermal statistics $E_n \equiv \langle N_s \rangle / \mathcal{M} \sim 0.1$. It can be seen as the number of photons per mode, and here is fixed, since we keep fixed (aside unwanted fluctuation pulse-to-pulse) the power of the laser. Therefore the multi-

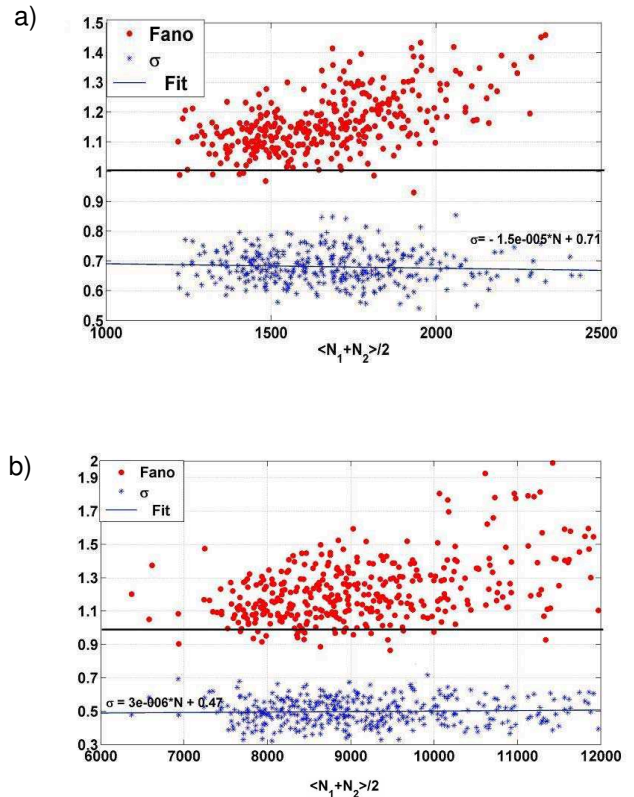


FIG. 2: Degree of Correlation and Fano factor versus the number of photons over a sample of 400 frames analyzed. Fig2(a) presents the data for binning 12×12 , i.e. a superpixel with size $(240\ \mu\text{m})^2$ and regions containing 320 superpixels. The mean value of correlation degree for this range of photon number is $\sigma = 0.681 \pm 0.003$ and the standard deviation of the sample is 0.06. The mean value of the Fano factor is $F = 1.17$ and the standard deviation of the population is 0.13. Fig2(b) presents the same analysis for binning 24×24 (superpixel size $(480\ \mu\text{m})^2$) and regions containing 56 superpixel. The mean value of correlation degree is $\sigma = 0.498 \pm 0.004$ and the standard deviation 0.08. Fano factor has mean value $F = 1.26$ and standard deviation of 0.35.

thermal statistics of the source in the single channel is quasi Poissonian, and this is confirmed by the Fano factors $F = 1 + E_n = \langle \delta^2 N_i \rangle / \langle N_i \rangle$ presented in Fig.2.

The first step of the measurement consists in evaluating the degree of correlation between pixel pairs belonging to large areas of PDC emission, without object. Chosen two correlated regions of PDC in the far field A_s and A_i of about $(3\text{mm})^2$ size, we evaluate the degree of correlation in Eq.(1) by performing spatial averages over the ensemble of correlated pixels belonging to the two regions. The measurement procedure is described in [23]. Fig.2 shows the results obtained for a sample of 400 images (each one corresponding to a pump shot and to a

point in the graphs) for the two binning size. In both cases the degree of correlation is well below the SNL. As expected, the result for binning 24x24 is better than for 12x12, and the last is better than the one reported in [23], anyway. Thus, we are in the regime $\sigma < 1$ needed for appreciating an improvement of the SSNQI with respect to the classical differential scheme.

IV. EXPERIMENTAL IMPERFECTION AND THEIR CORRECTION

In this section we aim to illustrate the experimental challenges for achieving a strong local sub-shot-noise correlation with a large number of detected photons over a large number of pixels at the same time. Actually working with high photon number is demanded for reducing the effect of the background. In fact the background (electronic noise of the CCD and straylight) can be corrected a posteriori on average, but the single image remains affected by this noise. Therefore we need to work in a condition of $\langle \delta^2 B \rangle / \langle \hat{N}_i + \hat{N}_s \rangle \ll 1$, where we indicate as B the number of background photons. The main sources of experimental excess noise are the following:

- 1) the intensity gradients in the regions $A_{s/i}$ of interest,
- 2) the error in the determination of the center of symmetry of the spatial correlation,
- 3) the background noise due to the straylight and the read-out noise of the CCD.

We analyze them in detail in the following subsections.

A. Intensity gradients

Up to now, we have considered an ideal situation in which the quantum efficiency η is constant and equal in the two optical paths.

From an experimental point of view, we had to cope with several sources of spatial dishomogeneity that contribute to the experimental excess noise and that can hide the quantum correlation, especially when large areas of PDC emission around degeneracy (710nm) are considered.

In the angular bandwidth corresponding to an area of $(3 \text{ mm})^2$ close to collinear direction, lies a frequency bandwidth of about 10-20 nm. The response of the filters and the CCD quantum efficiency have a frequency dependence even within this small range. This generates a spatial gradient in the intensity pattern. For instance the CCD sensitivity, that has a maximum around 800 nm, varies of about 3% in our range of wavelengths. The bandpass filter (see Fig.1) has a maximum of transmittance of 95% at 710 nm, decreasing of few parts percent at the border of our frequency region. These effects are even more complicated by the non-linear dependence of the frequency on the emission angle in the phase-matching function. Even the optical transmission at different angles can be influenced by the polarization.

Moreover, the spatial statistics of the detected light is affected by spatial imperfections of the optics, by the presence of dust and by the inhomogeneity of efficiency of the CCD pixels (a minor contribution). All these effects contribute to an increasing of the excess noise and, consequently, a deterioration of the noise reduction factor.

We modeled it by introducing a spatial dependence of the quantum efficiency $\eta_{j,k}$, with $j=s,i$ and k identifying the symmetrical pixels in the position \mathbf{x}_k and $-\mathbf{x}_k$ of the regions A_s and A_i respectively. The expectation values of the number of photons on the pixel k is:

$$\langle \hat{N}_{j,k} \rangle = \eta_{j,k} \langle \hat{n} \rangle \quad (4)$$

with $\langle \hat{n} \rangle$ the number of photon impinging a pixel in each frame. The associated variance and covariance are [29]

$$\langle \delta^2 \hat{N}_{j,k} \rangle = \eta_{j,k} \langle \hat{n} \rangle + \eta_{j,k}^2 \langle \hat{n} \rangle^2 / \mathcal{M} \quad (5)$$

$$\langle \delta \hat{N}_{s,k} \delta \hat{N}_{i,k} \rangle = \eta_{s,k} \eta_{i,k} (\langle \hat{n} \rangle + \langle \hat{n} \rangle^2 / \mathcal{M}). \quad (6)$$

Using Eq. (4), Eq. (5) and Eq. (6) in Eq. (1) we can calculate the theoretical value of the NRF:

$$\sigma_k = 1 - \eta_{+,k} + \frac{1}{2} \frac{\eta_{-,k}^2}{\eta_{+,k}} \left(\frac{\langle n \rangle}{\mathcal{M}} + \frac{1}{2} \right) \quad (7)$$

where $\eta_{+,k} = \frac{\eta_{s,k} + \eta_{i,k}}{2}$ is the mean value of the quantum efficiencies of signal and idler arm and $\eta_{-,k} = \eta_{s,k} - \eta_{i,k}$ is their difference. It is worth to observe that the degree of correlation is deteriorated by the unbalancing in the quantum efficiencies $\eta_{-,k}$ on the two paths. Due to the high pulse-to-pulse instability of the Q-switch laser, in our experiment it is convenient to estimate the NRF in the single frame obtained by a single laser shot. A single frame contains several pairwise spatial modes of the radiation, since the PDC is spatially broadband [16]; therefore, pixels belonging to regions A_i and A_s are pairwise correlated in the number of photons, and the pairs can be considered as independent if the condition $\mathcal{A}_{pix} \gg \mathcal{A}_{coh}$ is fulfilled. We estimate NRF as defined in Eq.(1), where the quantum mean values are evaluated by averages over the ensemble of the pixel pairs. The operator associated to the estimation of the mean photon number is

$$\hat{N}_j = \frac{1}{\mathcal{R}} \sum_{k=1}^{\mathcal{R}} \hat{N}_{j,k} \quad (8)$$

where \mathcal{R} is the number of pixels in the region. According to Eq. (4), the expected value of \hat{N} becomes

$$\langle \hat{N}_j \rangle = \frac{1}{\mathcal{R}} \sum_{k=1}^{\mathcal{R}} \eta_{j,k} \langle \hat{n} \rangle = \bar{\eta}_j \langle \hat{n} \rangle. \quad (9)$$

Similarly, the operator for the variance of the photon number is defined as:

$$\hat{S}_j^2 = \frac{1}{\mathcal{R}} \sum_{k=1}^{\mathcal{R}} (\hat{N}_{j,k} - \langle \hat{N}_j \rangle)^2 \quad (10)$$

Using Eq. (5), its expected value is $\langle \widehat{\mathcal{S}}_j^2 \rangle = \bar{\eta}_j \langle \hat{n} \rangle + (\bar{\eta}_j^2 + V(\eta_j)/\mathcal{M}) \langle \hat{n} \rangle^2 / \mathcal{M} + V(\eta_j) \langle \hat{n} \rangle^2$ (here we exclude correlation between the efficiency distribution in the two regions). We observe that performing the spatial statistics in order to estimate the theoretical quantities introduces a term of excess noise depending on the spatial variance $V(\eta_j)$ of the detection efficiency in the region A_j . At the same time, we can define the operator associated to the estimation of covariances as

$$\widehat{\mathcal{S}}_{s,i}^2 = \frac{1}{\mathcal{R}} \sum_{k=1}^{\mathcal{R}} (\hat{N}_{s,k} - \langle \hat{N}_s \rangle) (\hat{N}_{i,k} - \langle \hat{N}_i \rangle) \quad (11)$$

According to (6) and to (9), its expected value is $\langle \widehat{\mathcal{S}}_{s,i}^2 \rangle = \bar{\eta}_s \bar{\eta}_i \left(\langle \hat{n} \rangle + \frac{\langle \hat{n} \rangle^2}{\mathcal{M}} \right)$. Using the expectation values defined above, we can now estimate the experimental noise reduction factor:

$$\begin{aligned} \sigma^{exp} &= 1 - \bar{\eta}_+ + \frac{1}{2} \frac{\bar{\eta}_-^2}{\bar{\eta}_+} \left(\frac{\langle n \rangle}{\mathcal{M}} + \frac{1}{2} \right) + \\ &+ \left[\frac{V(\eta_s) + V(\eta_i)}{2\bar{\eta}_+} \right] \left(\langle n \rangle + \frac{\langle n \rangle}{\mathcal{M}} \right) \end{aligned} \quad (12)$$

Comparing the expected value of the NRF σ^{exp} estimated in the single frame with the theoretical value (7) that refers to the single pixel pair, a new term of excess noise depending on the spatial variance of the efficiency appears. Although the variance is usually rather small, this term can be relevant (even the dominant one) when the number of photons per pixel becomes as high as we deal in our working condition, and needs to be addressed.

This additional term can be corrected a posteriori by compensating the channel losses represented by $\eta_{j,k}$. Focusing, as usual, on the two regions of interests, the compensation consists in multiplying each matrix-image by a sort of "flat field" matrix $g_{j,k}$. This is obtained by the sum of \mathcal{Q} single shot images $F_{j,k} = \sum_{q=1}^{\mathcal{Q}} N_{j,k}^{(q)}$ normalized for the mean value in the region j as

$$g_{j,k}^{-1} = \frac{F_{j,k}}{\frac{1}{\mathcal{R}} \sum_{k=1}^{\mathcal{R}} F_{j,k}} = \frac{\eta_{j,k}}{\bar{\eta}_j}. \quad (13)$$

The flat field correction corresponds, in the theoretical model, to the substitution $N_{j,k} \rightarrow g_{j,k} N_{j,k}$ in the expressions (8), (10) and (11). Consequently, applying the flat field compensation as in Eq. (13), the experimental NRF becomes:

$$\sigma^F = 1 - \bar{\eta}_+ + \frac{1}{2} \frac{\bar{\eta}_-^2}{\bar{\eta}_+} \frac{\langle n \rangle}{\mathcal{M}} \quad (14)$$

that is a good estimation of the average NRF (7) over the two large regions. Thus, the application of this compensation for the losses disuniformity allows in principle to retrieve the expected quantum mean value of the NRF. Fig. 3 and Fig. 4 report the NRF and the Fano factor in

function of binning size and their values corrected by the flat field and for background noise. From the figures we notice that the effect of disuniformity, $V(\eta_j)$, dominates and the flat field correction becomes fundamental. In fact, an increasing of the superpixel size corresponds to an increment of the number of photons and, consequently, of the excess noise generated by $V(\eta_j)$ in Eq.(12). It is important to stress that this compensation is the same for all the images, since the transmission-detection efficiency distribution is always the same. Therefore, this technique can be applied successfully even in the imaging scheme, when an object is inserted.

B. Determination of the center of symmetry and sizing of the superpixel

We observe that the theoretical prediction $\sigma = 1 - \eta$ relies on the assumption that each pixel of \mathcal{A}_s detects all the spatial modes correlated to the ones collected by the corresponding pixel in \mathcal{A}_i , and viceversa. Otherwise, the presence of uncorrelated modes in the two regions would not provide a complete cancelation of the excess noise by the subtraction [31]. In particular it can be demonstrated that

$$\sigma' = 1 - \eta \frac{\mathcal{M}_c}{\mathcal{M}_c + \mathcal{M}_u} \left(1 - \frac{\mathcal{M}_u}{\mathcal{M}_c} E_n \right). \quad (15)$$

with $\mathcal{M}_{c/u}$ the number of spatial correlated/uncorrelated modes detected by a pair of symmetric pixels. When the center of symmetry (CS) is estimated exactly, $\mathcal{M}_u = 0$ and one retrieves the theoretical lower bound $\sigma' = \sigma$. Therefore, experimental precise positioning of the regions and accurate determination of the CS is fundamental. In [32] it is demonstrated by realistic simulation that an high level of correlation is obtained by finding the CS with sub-pixel resolution. In the present work the CS used in a measurement with a certain NxN binning grid (N=12 or N=24), is evaluated previously by using a more resolved grid (typically 2x2) as follows. Considering the region A_s we find the proper position of the correlated region A_i evaluating the noise reduction factor σ as a function of the position of A_i (moved by integer steps). The optimal position corresponds to a dip in the value of σ . Finally, taking two correlated pixels x_s and x_i , the center of symmetry is $x_c = \frac{|x_i - x_s|}{2}$. A different approach is based on a procedure of NRF optimization by micro-positioning of the CCD array [33].

However, for a given error in the determination of the CS, increasing \mathcal{A}_{pix} reduces the ratio between the uncorrelated and the correlated modes. Therefore, an appropriate determination of the minimum size of the superpixel can reduce this bias under an accepted threshold. Fig. 3 shows clearly a strong dependence of the NRF (after flat field correction) from the pixel size. This behaviour is well explained by a geometrical model based on Eq. (15).

C. Background noise

Another source of deterioration of the spatial correlations is the background noise. The two main sources of background noise are the electronic noise in the read-out and digitalization process and the straylight. The electronic noise of the CCD is $\Delta = 4$ photoelectron/pixel. This contribution can be strongly reduced in terms of signal to noise ratio when binning is performed. Straylight light is mainly due to the broadband fluorescence of the crystal, mirrors and filters hit by the strong UV pulse of the laser and to the residual UV light itself. The background noise can be estimated independently by acquiring an image without PDC light, simply by rotating the pump polarization of 90 degrees. The experimental value of the NRF (1) can be corrected a posteriori taking into account the mean value of the background:

$$\sigma^B = \frac{\langle \delta^2(\hat{N}_i - \hat{N}_s) \rangle - \langle \delta^2 B_s \rangle - \langle \delta^2 B_i \rangle}{\langle \hat{N}_i + \hat{N}_s \rangle - \langle B_s + B_i \rangle} \quad (16)$$

where $\langle B_j \rangle$ is the mean photon numbers of the area A_j of the background image and $\langle \delta^2 B_j \rangle$ is its variance. The same correction can be applied to the Fano factors. From Fig. 3 we notice that the electronic noise is the main source of deterioration of sigma for low binning size (small \mathcal{A}_{pix}), while for larger binning the effect of disuniformity, $V(\eta_j)$, dominates. This can be explained considering that the read-out noise of the pixel (or superpixel) is a fixed value, independent on the binning. Nonetheless larger superpixels detect more photons, reducing the effect of read-out noise ($\langle \delta^2 B_j \rangle / \langle \hat{N}_j \rangle \ll 1$). The same considerations are valid for the Fano factors (Fig.4). The straylight collected per superpixel is expected to have a Poissonian-like statistics and obviously increases with the binning together with the PDC light. Therefore, its contribution, and the relative correction in the graphs, should be independent on binning.

We want to stress once again that, differently from the case of the flat field correction, the background can be corrected on average, but the single image remains affected by its noise. Thus, one can not apply any correction for the background noise to the SSNQi scheme.

V. QUANTUM VS CLASSICAL IMAGING

We insert a weak absorbing object in the signal beam region R_s . It is a thin (less than 10nm) titanium deposition of 9mm² area on a glass, representing a π . The SSNQi image of the object is obtained by subtracting from the direct image registered in the signal branch, the correlated intensity noise pattern registered in the idler branch, as it is depicted in the left side column of Fig.5(a) for binning 12x12 and Fig.5(b) for binning 24x24. In order to compare the results of the quantum scheme with

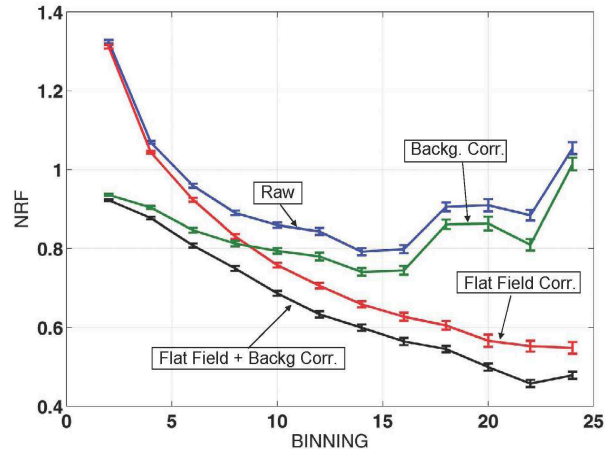


FIG. 3: The plot reports the value of the Noise Reduction Factor as a function of binning size N. The red (continuous) line refers to raw data, without any noise correction. The corresponding data after the background subtraction are reported in the green (dashed) line. The red (dotted) line refers to data corrected with Flat Field and the black (dotted dashed) line data takes into account both Flat Field and background corrections.

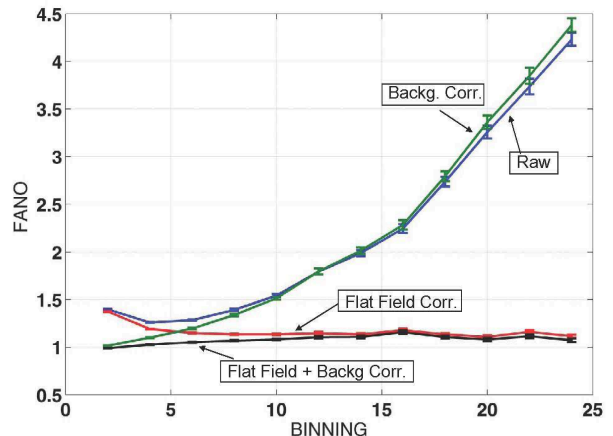


FIG. 4: The plot reports the value of the Fano factors as a function of the binning size N. The colors are according to Fig. 3

the corresponding DCI scheme, we simulate the last one by subtracting from the direct image a noise pattern that is not correlated at the quantum level with the one containing the object (see right side of Fig.5 (a) and (b)). It is obtained simply by choosing a region belonging to the idler field that is shifted by at least one pixel with respect the quantum correlated one. In order to simulate a coherent illumination in both branches, the experimental spatial noise in the region A_s and A_i should obeys to a Poissonian statistics, i.e. it should be shot noise lim-

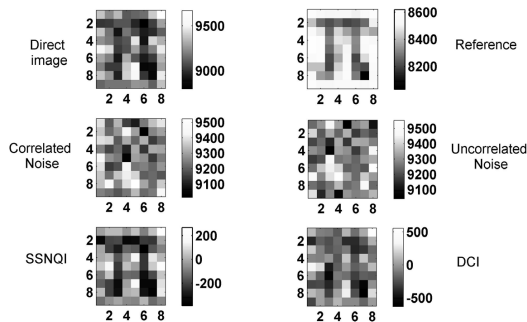
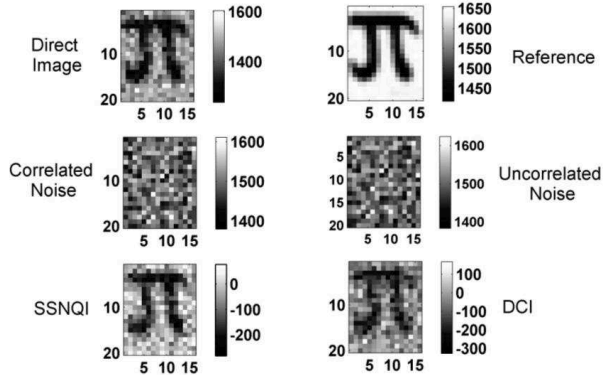


FIG. 5: Experimental imaging using correlated properties of PDC quantum light, where the color-map is associated with the selected photon number as reported on the righthand side of each image. In (a) the pixel size is $(240\mu m)^2$ and the absorption coefficient of the object is around $\alpha = 12\%$. In (b) we use less absorbing object with $\alpha = 5\%$ and pixel size of $(480\mu m)^2$ (see the text for discussion).

ited. As we discussed above, in our working condition the low gain and the large number of collected modes limit the spatial excess noise of the single beams to small values (see Fano factor in Fig.2 and Fig.4). Furthermore, we report the images obtained by direct classical imaging, that in the present configuration represents the best possible classical scheme. By observing Fig.5, it is quite evident an improvement of the SSNQI image both with respect to the DCI and direct classical one. In the case of larger binning in particular, the object in the DCI image is even undistinguishable ($\alpha = 5\%$), whereas it is well perceivable in the SSNQI frame. There is always a trade-off between the need of enlarging the detection areas for more squeezing effect, and to preserve, at the same time the spatial resolution of the image. In fact this is just

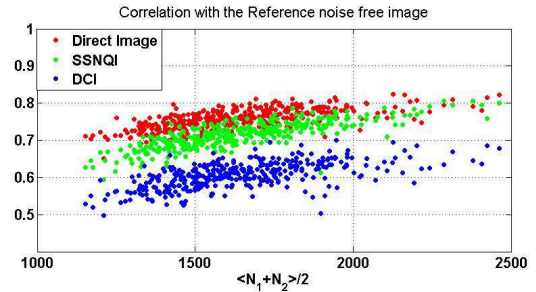


FIG. 6: Correlation coefficient between a reference noise free image and the single shot frame over 400 frames. Fig. 4 present the results for the 12x12 binning: the mean correlation coefficients are $C_{SSQNI} = 0.71$, $C_{DCI} = 0.60$, $C_{direct} = 0.75$ respectively for the quantum, the differential classical, and the direct imaging.

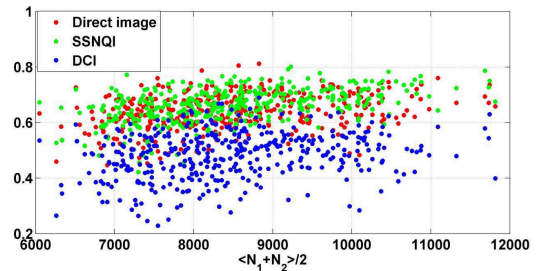


FIG. 7: Correlation coefficient between a reference noise free image and the single shot frame over 400 frames. Fig. 5 present the results for the 24x24 binning: the mean correlation coefficients are $C_{SSQNI} = 0.664$, $C_{DCI} = 0.483$, $C_{direct} = 0.641$ respectively for the quantum, the differential classical, and the direct imaging, with statistical uncertainty smaller than 10^{-3}

a technical problem, that in principle can be solved by using larger diameter of the pump laser and crystals.

In order to quantify rigorously the improvement in the sensitivity of the SSNQI, we consider two different figures of merit.

A. Correlation function

The first one consists in creating a noise free reference image of the object, and to compare the SSNQI and the

classical (DCI and direct) images against the reference one. Operatively, the noise free image can be prepared by averaging over a large number of direct images, so that almost all the noise, due to multi-thermal statistics of light as well as to the electronics of the digitalization process, is washed away. The obtained reference images for the two binning conditions are reported in Fig.5. The comparison of the SSNQI and the classical schemes against the reference is quantified by the square correlation coefficient

$$C_j = \frac{\langle \delta \mathcal{I}_j(\mathbf{x}) \delta \mathcal{I}_{ref}(\mathbf{x}) \rangle^2}{\langle \delta^2 \mathcal{I}_j(\mathbf{x}) \rangle \langle \delta^2 \mathcal{I}_{ref}(\mathbf{x}) \rangle} \quad (17)$$

where $j = SSNQI, DCI$, $\mathcal{I}_{SSNQI}(\mathbf{x}) = N_i(-\mathbf{x}) - N'_s(\mathbf{x})$ and $\mathcal{I}_{DCI}(\mathbf{x}) = N_i(-\mathbf{x} + \mathbf{a}) - N'_s(\mathbf{x})$. \mathbf{a} is the shift vector and the prime (') indicates the number of photons detected in presence of the object. In principle the image that retains more detail of the object, inspite the deterioration due to the noise, has a larger correlation value C_j . For instance, for the images of Fig.5(b) we have $C_{SSNQI} = 0.56$, $C_{DCI} = 0.41$, $C_{direct} = 0.49$.

The analysis has been performed on a sample of 400 images and the results are reported in Fig.6 for binning 12x12 and Fig.7 for binning 24x24. The correlation coefficient of the SSNQI (green marks) is always larger than the one for DCI (blu marks). In order to be completely fair one could take into account a sample of images that presents a null excess noise on average, i.e. a Fano factor exactly equal to 1.0 on average. In fact we did, and the results do not differ from the behavior of the data presented in Fig 6 in the region of low photon number. As expected, for the larger superpixel size, the discrimination between the classical and the quantum imaging is more pronounced although more spread. This is related with the degree of correlation that increases with the detection areas, as we have seen in Sec.III. In the case of large pixel size, the SSNQI result is even better than the direct image obtained in the signal branch. This is in agreement with the value of the correlation degree that in the last case is smaller than 0.5 (see caption of Fig. 5(b)). This is the evidence that the method could become in the future a real tool for low noise imaging, whenever a small illumination level is needed.

B. SNR

The second figure of merit that we consider is strictly related to the theoretical Eq.(3). It consists in measuring the signal to noise ratio in the classical imaging and in the quantum imaging schemes and to compare them. For the following analysis it is convenient to insert in the signal beam an object with a uniform absorption $\alpha(\mathbf{x}) = \alpha \sim 5\%$, i.e. a square shaped deposition that can be considered having a constant thickness for our purposes. The prediction of Eq. (3) are tested on a

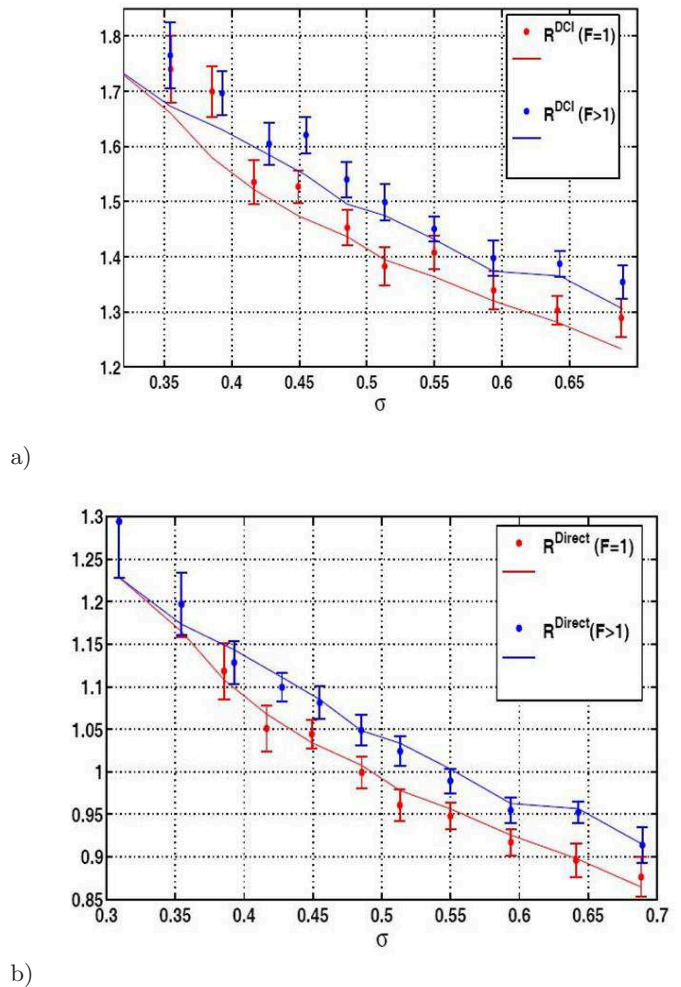


FIG. 8: (a) R^{DCI} of the SNR in the SSNQI scheme and in the DCI scheme for binning 24x24. The blue marks represent the result that take in to account all the frames, without selection on the Fano factor, while the red marks are obtained taking into account only images that have Fano factors of $F = 1 \pm 0.2$ (b) R^{Direct} of the SNR in the SSNQI scheme and in the Direct scheme. The lines represent the theoretical predictions

large number of frames (about 1200) for the case of binning 24x24 and 32x32. We group the frames in classes with respect to their value of σ , estimated for each image as described in Sec. III. Belonging to the j -class are the images with degree of correlation falling in a small band (bandwidth=0.1) with average σ_j and average Fano factor F_j . The estimation of the absorption spatial distribution in the SSNQI scheme is obtained by following the Eq. (2). Experimentally, for the generic k -th image belonging to the j -th class we perform the subtraction $(N_i^{(k)}(-\mathbf{x}) - N'_s^{(k)}(\mathbf{x})) / \langle N_i^{(k)} \rangle \equiv \alpha_k(\mathbf{x})$ between signal and idler correlated pattern and $\langle N_i^{(k)} \rangle = \sum_{\mathbf{x}} N_i^{(k)}(-\mathbf{x})$. Then the value of $\alpha(\mathbf{x})$ is obtained averaging over the

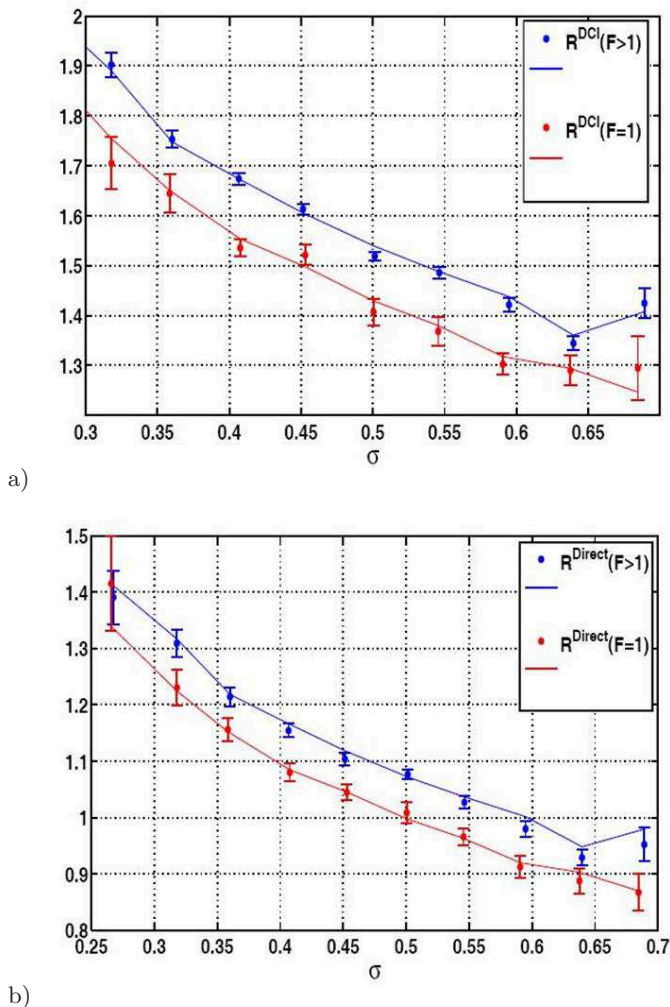


FIG. 9: (a) R^{DCI} of the SNR in the SSNQI scheme and in the DCI scheme for binning 32x32. The blue marks represent the result that take in to account all the frames, without selection on the Fano factor, while the red marks are obtained taking into account only images that have Fano factors of $F = 1 \pm 0.2$ (b) R^{Direct} of the SNR in the SSNQI scheme and in the Direct scheme. The lines represent the theoretical predictions

frames of the j -th class, i.e.

$$\alpha(\mathbf{x}) = \frac{1}{\mathcal{N}_j} \sum_{k=1}^{\mathcal{N}_j} \alpha_k(\mathbf{x}) \equiv \overline{\alpha_k(\mathbf{x})} \quad (18)$$

where \mathcal{N}_j is the number of images in the j -th class.

The differential classical scheme with coherent beam can be simulated in our set-up by evaluating the absorption as in the previous Eq. (18) where the region of the idler is slightly shifted from the quantum correlated one $N_i(-\mathbf{x} + \mathbf{a})$ (typically we take $\mathbf{a} = (1, 0)$).

For each class, the SNR for the quantum and for the classical schemes can be estimated punctually as $SNR_j(\mathbf{x}) = \overline{\alpha_k(\mathbf{x})} / [\overline{\delta^2 \alpha_k(\mathbf{x})}]^{1/2}$, where the overline indicates the average over the frames of the class j .

At the same time we evaluate the factor $R_j^{DCI}(\mathbf{x}) = SNR_j^{SSNQI} / SNR_j^{DCI}$. Then, we perform also a spatial averages over \mathbf{x} , to obtain a representative value of R_j^{DCI} for each class. The results are shown in Fig.8(a) and Fig.9(a) against the correlation degree σ_j for the binning 24x24 and 32x32 respectively: the SSNQI has, as expected, an advantage that increases with the level of correlation. Selecting only images with Fano factors very close to 1 for simulating a classical coherent illumination (red data-set), the result are just slightly worse as one without Fano selection (blu data-set). However, for the best achieved values of the correlation degree in the quantum regime, we obtain an improvement of the SNR larger than than 70% compared with the classical imaging scheme. The results are in agreement with the theoretical predictions obtained by the generalization of Eq. (3) with the substitutions $E_n^{class} \rightarrow F_j - 1$ and $\sigma \rightarrow \sigma_j$.

In Fig. 8(b) and Fig.9(b) we report the Ratio R of the SNR in the SSNQI scheme and in the direct classical scheme. When Fano values are selected to be ~ 1 (red data-set), allowing a proper simulation of a shot noise limited classical imaging, the results are in perfect agreement with what expected from theory. In particular for small α , we have $R = \frac{1}{\sqrt{2\sigma}}$, i.e. the SSQI overcomes the direct classical imaging as soon as $\sigma < 0.5$.

VI. CONCLUSION

We have presented the first experimental quantum imaging protocol aimed to improve the sensitivity of imaging techniques beyond the shot-noise-limit, that represents the threshold between classical and quantum world. We reached a considerably high level of multi-mode spatial correlations using the properties of twin beams generated by the parametric-down-conversion process, and we used it for reducing the noise in the differential imaging scheme. Our results represent the proof of principle of this new quantum technology. Anyway, some technical limitation toward practical application of the methods are still present in our setup. Firstly, total transmission of the optical channel should be improved in order to reach even higher quantum correlations. Furthermore, there is always a tradeoff between the need of enlarging the detection areas for more squeezing effect, and at the same time to preserve the spatial resolution of the image. In fact this is just a technical problem, that in principle can be solved by reducing the coherence area of the single spatial mode, in particular using larger diameter of the pump laser and crystals. A work for solving these problems in view of practical applications is now going on [26].

VII. ACKNOWLEDGEMENTS

This work has been supported by PRIN 2007FYETBY (CCQOTS). Thanks are due to E.Monticone and C.

Portesi for the thin film deposition representing the weak absorbing object, to P. Cadinu for help in the data anal-

ysis and to A. Gatti, E. Brambilla, L. Caspani and L. Lugiato for theoretical support.

-
- [1] M. Genovese, Research on hidden variable theories: a review of recent progresses. *Phys. Rep.* 413, 319 (2005) and ref.s therein.
- [2] Marcikic, I., de Riedmatten, H., Tittel, W., Zbinden, H., Legr, M., and Gisin N., Distribution of Time-Bin Entangled Qubits over 50 km of Optical Fiber, *Phys. Rev. Lett.* 93, 180502 (2004).
- [3] Tiefenbacher, F., Schmitt-Manderbach, T., Weier, H., Scheidl, T., Lindenthal, M., Blauensteiner, B., Jennewein, T., Perdigues, J., Trojek, P., Mer, B., et al. Entanglement-based quantum communication over 144 km. *Nature Physics* 3, 481-486 (2007).
- [4] Bouwmeester, D. et al. Experimental quantum teleportation. *Nature* 390, 575 (1997).
- [5] Jennewein, T., Aspelmeyer, M., Kaltenbaek, R., Lindenthal, M., Walther, P., Zeilinger, A., Ursin, R. Communications: Quantum teleportation across the Danube *Nature* 430 849-849 (2004)
- [6] Boschi, D., Branca, S., De Martini, F., Hardy, L. and Popescu S., Experimental Realization of Teleporting an Unknown Pure Quantum State via Dual Classical and Einstein-Podolsky-Rosen Channels. *Phys. Rev. Lett.* 80 1121 (1998) .
- [7] O'Brien, J.L., Optical Quantum Computing, *Science* 318 1567 (2007).
- [8] Kwiat, P.G. et al., Experimental entanglement distillation and hidden non-locality. *Nature* 409 1014 (2001).
- [9] Yamamoto, T. et al., Experimental extraction of an entangled photon pair from two identically decohered pairs. *Nature* 421 343 (2003).
- [10] Pan, J.W. et al., Entanglement purification for quantum communication. *Nature* 410 1067 (2001).
- [11] Pan, J.W. et al., Experimental entanglement purification of arbitrary unknown states, *Nature* 417 4174 (2003).
- [12] Lugiato, L.A., Gatti, A. and Brambilla, E., Quantum Imaging, *J. Opt. B Quant. Semiclass. Opt.* 4 S176 (2002) and ref.s therein.
- [13] Boyer, V. et al., Entangled Images from four-wave mixing. *Science* 321 544 (2008).
- [14] Brambilla, E., Caspani, L., Jedrkiewicz, O., Lugiato, L.A and Gatti, A. High-sensitivity imaging with multi-mode twin beams. *Phys. Rev. A.* 77 053807 (2008).
- [15] Quantum Imaging, Kolobov editor (Springer, New York, 2007), and ref.s therein.
- [16] Brambilla, E., Gatti, A., Bache, M., and Lugiato L. A. Simultaneous near-field and far-field spatial quantum correlations in the high-gain regime of parametric down-conversion. *Phys. Rev. A* 69, 023802 (2004).
- [17] Giovannetti, V., Lloyd, S., Maccone, L., Quantum Metrology. *Phys Rev. Lett.* 96, 010401 (2006).
- [18] Ruo Berchera, I. Theory of PDC in a Continuous Variables Framework and its Applications to the Absolute Calibration of Photo-Detectors, *Adv. Sci. Lett.* 2, 407 (2009).
- [19] Nabors, C.D., and Shelby, R.M., Two-color squeezing and sub-shot-noise signal recovery in doubly resonant optical parametric oscillators *Phys. Rev. A* 42 556 (1990).
- [20] Tapster, P.R., Seward, S.F., and Rarity, J.G., Sub-shot-noise measurement of modulated absorption using parametric down-conversion, *Phys. Rev. A* 44 3266 (1991).
- [21] Souto Ribeiro, P.H., Schwob, C., Maitre, A. and Fabre, C., Sub-shot-noise high-sensitivity spectroscopy with optical parametric oscillator twin beams *Opt. Lett.* 22 1893 (1997).
- [22] Bondani, M., Allevi, A., Zambra, G., Paris, M. and Andreoni, "A. Sub-shot-noise photon-number correlation in a mesoscopic twin beam of light", *Phy. Rev. A* 76, 013833 (2007); T. Ishkakov, M. Chekhova, G. Leuchs, "Generation and Direct Detection of Broadband Mesoscopic Polarization-Squeezed Vacuum", *Phys. Rev. Lett.* 102, 183602 (2009).
- [23] Brida, G., Caspani, L., Gatti, A., Genovese, M., Meda, A., and Ruo Berchera, I. Measurement of sub-shot-noise spatial correlations without background subtraction. *Phys Rev. Lett.* 102, 213602 (2009).
- [24] Jedrkiewicz, O. et al., Detection of Sub-Shot-Noise Spatial Correlation in High-Gain Parametric Down Conversion *Phys. Rev. Lett.* 93 243601 (2004).
- [25] G. Brida, M. Genovese, I. Ruo Berchera, *Nature Photonics* 4 (2010) 227.
- [26] I. Ruo Berchera et al., work in progress.
- [27] Brida, G., Genovese, M., Meda, A., Predazzi, E. and Ruo Berchera, I., Systematic study of the PDC speckle structure for quantum imaging applications. *Int. Journ. Quant. Inf.* 7 139 (2009).
- [28] Brida, G., Genovese, M., Meda, A., Predazzi E. and Ruo Berchera, I., Tailoring PDC speckle structure. *Journal of Modern Optics* 56 201 (2009).
- [29] In a single pixel k are collected \mathcal{M} modes of the radiation. Since the mean value of the number of photon per modes $\langle \hat{n}_m \rangle$ is considered as constant, the average number of photon per pixel is $\langle \hat{n} \rangle = \sum_{m=1}^{\mathcal{M}} \langle \hat{n}_m \rangle = \mathcal{M} \langle \hat{n} \rangle$. Assuming that the modes are statistically independent and that the number of photons per mode in each branch obeys to a thermal statistics [30], its variance is: $\langle \delta^2 \hat{n} \rangle = \sum_{m=1}^{\mathcal{M}} \langle \delta^2 \hat{n}_m \rangle = \mathcal{M} \langle \delta^2 \hat{n} \rangle = \mathcal{M} \langle \hat{n} \rangle (1 + \langle \hat{n} \rangle) = \langle \hat{n} \rangle \left(1 + \frac{\langle \hat{n} \rangle}{\mathcal{M}} \right)$.
- [30] Mandel, L., and Wolf E., *Optical Coherence and Quantum Optics*, (Cambridge University Press, Cambridge, 1995).
- [31] Agafonov, I. N., Chekhova, M. V., Leuchs, G., Two-Color Bright Squeezed Vacuum, arXiv:0910.4831.
- [32] Caspani, L. et al., Improving the observation of spatial quantum correlation of twin beams by means of a sub-pixel symmetry centre retrieval algorithm *Journ. Mod. Opt.*, 55, 13 (2008).
- [33] Brida, G., Degiovanni, I.P., Genovese, M., Rastello, M.L., Ruo Berchera, I. Detection of multimode spatial correlation in PDC and application to the absolute calibration of a CCD camera, arXiv 1005.2937 .